Chemical Papers (2020) 74:4581–4592
https://doi.org/10.1007/s11696-020-01275-2

ORIGINAL PAPER

Promotional effect of nickel addition on soot oxidation activity of $Ce_{0.9}Pr_{0.1}O_2$ oxide catalysts

Kirti Rajvanshi[1] · Sunaina S. Patil[1] · Lakhanlal[1] · Hari Prasad Dasari[1] · M. B. Saidutta[1] · Harshini Dasari[2]

Received: 13 March 2020 / Accepted: 29 June 2020 / Published online: 6 July 2020

Abstract

The present study investigates the promotional effect of Ni addition on soot oxidation activity of $Ce_{0.9}Pr_{0.1}O_2$ oxide catalysts. A series of *x*Ni-PDC (*x*= 0, 3, 5, 7, 10, 15, and 20 mol%) catalysts were synthesized by solution combustion synthesis method and characterized by XRD, Raman spectroscopy and TEM analysis. XRD and SAED patterns of the catalysts show cubic fluorite structure of ceria with an average crystallite size of 6–8 nm, and only 20Ni-PDC display NiO as a secondary phase. Raman spectra of *x*Ni-PDC catalysts display an increase in oxygen vacancies. With a minimum addition of 10 mol% Ni to PDC, i.e., the 10Ni-PDC catalyst showed optimum soot oxidation activity (T_{50} = 360 °C) than compared to PDC and other Ni-PDC catalysts. Lattice strain and oxygen vacancies played a key descriptor role in showing better soot oxidation activity of the 10Ni-PDC catalyst. From the soot oxidation kinetic studies, the activation energy obtained by Ozawa plots for the 10Ni-PDC catalyst is 137 kJ/mol.

Keywords Praseodymium-doped ceria · Nickel doping · Soot oxidation activity · Activation energy · Ozawa plots

Introduction

Diesel engines, due to their higher power generation capability and good fuel economy, are extensively used in the transportation sector, especially in heavy-duty vehicles (Xin 2013). Particulate matter, i.e., soot produced during partial combustion of diesel fuel in fuel dense regions of the diesel engine (Pischinger et al. 1994) is a major contributor to air pollution and global warming (Ramanathan and Carmichael 2008) and is responsible for respiratory and cardiovascular diseases (Sydbom et al. 2001; Ristovski et al. 2012). Diesel particulate filter, an automotive exhaust emission control technology, traps soot from the exhaust of diesel engine and requires regeneration to avoid backpressure build-up due to blockage, which otherwise may adversely impact engine operation. Since soot ignites around 600 °C and the temperature of exhaust gases is much lower than 600 °C (Adler 2005), appropriate soot oxidation catalysts need to be developed to burn off soot at lower temperatures (Bueno-López et al. 2005; Andana et al. 2016).

CeO_2 has been intensely researched for its catalytic activity in soot oxidation reactions. The exceptional redox properties of ceria (Ce^{3+}/Ce^{4+}) allow uptake and release of oxygen in oxygen-rich and lean conditions, respectively, resulting in good oxygen storage capacity (Setiabudi et al. 2004; Bueno-López et al. 2005; Machida et al. 2008). Gaseous oxygen may adsorb in the anionic vacancies of ceria forming active oxygen species, which react more spontaneously with soot as compared to gaseous oxygen and hence enhances soot oxidation reaction rate (Bueno-López et al. 2005). However, at high temperatures, it has been reported that aggregation of ceria leads to a reduction in surface area and changes its redox property and oxygen storage capacity (Atribak et al. 2008; Mukherjee and Reddy 2018). Incorporation of suitable dopants, like noble, transition and rare earth elements (Pt, Pd, Ru, Ag, Mn, Cu, Co, Fe, Zr, La, Pr, Hf, Gd, and Nd) into the ceria lattice helps to modify properties like thermal stability, reducibility, and oxygen mobility of ceria to enhance soot

Electronic supplementary material The online version of this article (https://doi.org/10.1007/s11696-020-01275-2) contains supplementary material, which is available to authorized users.

✉ Hari Prasad Dasari
energyhari@nitk.edu.in

[1] Chemical Engineering Department, National Institute of Technology Karnataka, Mangalore 575025, India

[2] Chemical Engineering Department, Manipal Institute of Technology, Manipal Academy of Higher Education (MAHE), Manipal 576104, India

oxidation activity (Bueno-López 2014; Liu et al. 2015; Andana et al. 2016; Mukherjee et al. 2016; Anantharaman et al. 2018; Patil et al. 2019). As per literature, noble metal (Ag, Ru, Pt, and Pd) supported ceria-based catalysts have been widely investigated in soot oxidation reactions (Aneggi et al. 2009; Kayama et al. 2010; Lim et al. 2011; Nascimento et al. 2014). Good metal-support interactions have shown to improve the reducibility of ceria and generate more active oxygen species, resulting in improved soot oxidation catalytic activity (Grabchenko et al. 2020). However, high cost and lesser availability of noble metals have encouraged research for other effective catalysts. Transition metals (Co, Cu, Fe, and Mn) on ceria-based support are studied for soot oxidation reaction as catalysts (Rao et al. 2011; Venkataswamy et al. 2014; Zhang et al. 2016; Xu et al. 2017). Due to the synergetic effect obtained by the addition of transitional metals to ceria-based catalysts, better catalytic performance is obtained in several oxidation reactions (Shen et al. 2013; Giménez-Mañogil et al. 2014; Sudarsanam et al. 2015; Putla et al. 2015).

Nickel-based catalysts are used to catalyze reactions like methane combustion reaction due to large oxygen adsorption capacity of NiO catalysts (Liu et al. 2017), water oxidation (Singh et al. 2013), CO oxidation (Singhania and Gupta 2017) and partial oxidation of methane (Alvarez-Galvan et al. 2019) reactions and are also used in fuel electrodes of solid oxide cells (Hauch et al. 2016). Recent studies on the Nickel-incorporated soot oxidation catalysts reported in the literature, such as $Ni_xCo_{3-x}O_4$ spinel catalyst (Zhao et al. 2019), $Mn_{1.9}Ni_{0.1}O_{3-\delta}$ (Neelapala et al. 2018), $Ni/CoAl_2O_4$ spinel (Álvarez-Docio et al. 2020) and $SrMn_{0.98}Ni_{0.02}O_3$ perovskite catalysts (Uppara et al. 2019) have shown improved soot oxidation activity on nickel incorporation. Nickel incorporation in ceria lattice has also shown to have a positive impact on the soot oxidation activity of ceria (Bendieb Aberkane et al. 2019) due to an increase in the oxygen vacancies.

According to literature (Thrimurthulu et al. 2012; Guillén-Hurtado et al. 2015, 2020; Andana et al. 2016; Mukherjee et al. 2016), praseodymium-doped ceria performs better than pure ceria in catalyzing soot oxidation reactions. The addition of praseodymium as a dopant in ceria enhances the redox properties, leading to an increased number of oxygen vacancies (Andana et al. 2016; Guillén-Hurtado et al. 2020) and lattice oxygen mobility and also improves the thermal stability of ceria through solid solution formation (Thrimurthulu et al. 2012; Zhou et al. 2018). Effect of morphologies such as nanorod, nanocube, nanofiber (Andana et al. 2016; Jeong et al. 2019), and the effect of variation in Ce/Pr composition (Guillén-Hurtado et al. 2020) on soot oxidation activity have been extensively investigated. Copper loaded (Rico-Pérez et al. 2016) and Pt-impregnated (Andana et al. 2018) ceria-praseodymium mixed oxides have been investigated in literature for catalyzed soot oxidation reactions.

In the present study, different compositions of Nickel-modified praseodymium-doped ceria (xNi-PDC) ($x = 0$, 3, 5, 7, 10, 15, and 20 mol%) catalysts were synthesized by solution combustion synthesis (SCS) method and are studied for their catalytic activity towards diesel soot oxidation reaction.

Experimental

xNi-PDC ($x = 0$, 3, 5, 7, 10, 15, and 20 mol%) catalysts were synthesized by SCS method using glycine. Nickel Nitrate Hexahydrate (98%, Loba Chemie), Praseodymium (III) Nitrate Hexahydrate (99.9%, Aldrich), and Cerous Nitrate Hexahydrate (99.9%, SRL chemicals) were mixed in the stoichiometric ratio in water with continuous stirring and heating at 80 °C. Glycine (99.5%, SRL chemicals) was added to the mixture in the stirring condition with glycine to nitrate ratio as 0.12. The detailed synthesis procedure of solution combustion synthesis is similar to our earlier reports (Patil et al. 2019). The mixture was heated until a green-colored viscous gel was obtained and further heated at 250 °C in a hot air oven. The oven-dried powder obtained is calcined at 500 °C/2 h to obtain the desired xNi-PDC catalysts.

Characterization

The obtained catalysts were characterized by X-ray Diffraction (XRD, XPERT Pro diffractometer), Raman spectroscopy (Bruker RFS 27), high-resolution transmission electron microscopy (HR-TEM- JEOL/JEM 2100), and selected area electron diffraction (SAED) techniques as described in our earlier reports (Patil et al. 2019). XRD was carried out with Cu Kα radiation ($\lambda = 0.1540$ nm) operating at 40 kV and 30 mA with 20°–80° 2θ range. Mean crystallite size (D) is determined using Scherrer's equation [$D = 0.9\lambda/\beta \bullet \cos\theta$] and lattice strain ($\varepsilon$) is calculated using the Williamson-Hall equation [$\varepsilon = \beta/(4\tan\theta)$] (Bindu and Thomas 2014; Govindhan et al. 2018), where D is the crystallite size, λ is the wavelength of radiation, θ is the peak position, and β is the corrected peak width at half maximum intensity. Raman Spectroscopy with a 532 nm laser beam in the range of 200–3000 cm^{-1} wavelength was used to study the vibrational modes and oxygen vacancies present in the sample. HR-TEM with SAED analysis was used to understand the microstructure and morphology of the samples.

The soot oxidation experiment to evaluate the catalytic activity of samples was performed in thermogravimetric analysis equipment (TGA, TG–DTA 6300) as described in our previous report (Shenoy et al. 2019). TGA was operated up to 650 °C in an air atmosphere at a flow rate of 100 ml/min at a heating rate of 10 °C/min. Soot (Printex-U, Orion Engineered Chemicals) and *x*Ni-PDC catalysts were mixed in a 1:10 ratio using electric mortar and pestle in tight contact mode for 30 min. The following formula is used for soot conversion (Zeng et al. 2020).

$$\text{Soot conversion} = \left[\left(W_i - W_o\right)/\left(W_i - W_e\right)\right] \times 100$$

where, W_i is the initial sample weight, W_e is weight after the heating and W_o is the weight at each temperature point.

The soot oxidation kinetic data of PDC, 5Ni-PDC and 10 Ni-PDC catalysts is obtained at various constant heating rates (5, 10, 15 and 20 °C/min) and the activation energy is calculated using Ozawa equation [$\log \beta = B - 0.4567\ (E_a/RT_\alpha)$] (Zeng et al. 2020), where β is the constant heating rate, T_α is the absolute temperature at conversion α, E_a is the activation energy, B is a constant and R is the universal gas constant. A plot of log β versus $1/T_\alpha$ graph gives a straight line for each percentage conversion (20, 30, 40, 50, 60, 70, 80, and 90%), and apparent activation energy can be calculated from the slope.

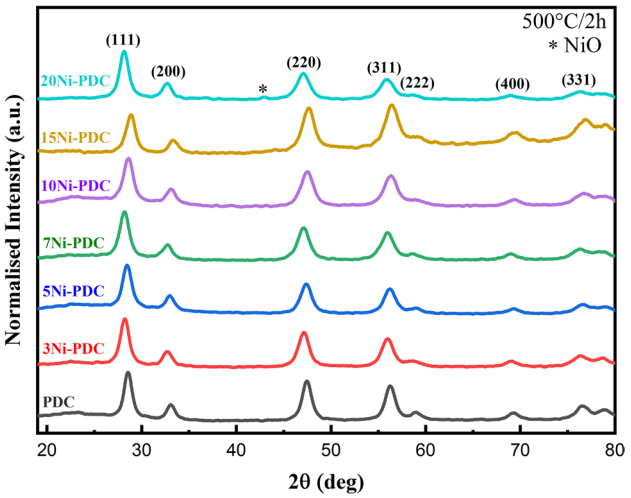

Fig. 1 XRD patterns of all Ni-PDC samples synthesized by SCS calcined at 500 °C/2 h in air

Results and discussion

XRD patterns of *x*Ni-PDC catalysts synthesized by SCS and calcined in air at 500 °C/2 h are shown in Fig. 1, and the peaks correspond to the cubic fluorite structure of ceria (Chen and Chang 2005; Tok et al. 2007; Zhou et al. 2016). The peaks related to Ni ($2\theta = 44.4°$, 51.8°, 76.4°) (Miniach et al. 2016)/NiO ($2\theta = 37.28°$, 43.3°, 62.8°, 75.3) (Venugopal et al. 2007) and PrO_2 ($2\theta = 28.6°$, 33.2°, 47.6°, 56.5°, 59.3°, 69.6°) (Yadav et al. 2011)/Pr_2O_3 ($2\theta = 26.6°$, 29.7°, 30.5°, 40.3°, 47.0°, 53.2°, 56.6°, 57.2°) (Lo Nigro et al. 2003)/Pr_6O_{11} ($2\theta = 28.25°$, 32.739°, 46.995°, 55.707°, 58.426°, 68.590°, 75.735°, 78.085°) (Abu-Zied et al. 2013; Matović et al. 2013) were not observed up to 15 mol% nickel doping in PDC samples, indicating Ni–Ce–Pr–O solid-solution formation. For the 20Ni-PDC catalyst, a small peak is observed at $2\theta = 42.95°$, which is attributed to the nickel oxide phase (Ding et al. 2018), indicating that some of the Nickel added as a dopant is present as NiO. Table 1 tabulates the crystallite size and lattice strain data of *x*Ni-PDC catalysts. The average crystallite size varies from 6 to 8 nm for all catalysts. With the addition of Ni up to 7 mol%, as a dopant in PDC, the lattice strain is increased from 0.0131 to 0.0167. With a further 10–20 mol% increase in nickel content, the lattice strain is almost constant. Thus, it can be inferred that the addition of Ni from 10–20 mol% resulted in no significant change in lattice strain. In general, an increase in lattice strain due to lattice distortion on the incorporation of dopant results in better oxygen diffusion and oxygen migration, which enhances the oxidation reaction (Kehoe et al. 2011; Rushton and Chroneos 2014). The facet ratios, [100]/[111] and [110]/[111] were calculated and tabulated in Table 1. [100]/[111] is found to increase up to 10 mol%

Table 1 Crystallite size, lattice strain, XRD peak intensity ratios, Raman peak intensity ratio and T_{50} of all Ni-PDC samples synthesized by SCS and calcined in air at 500 °C/2 h

Sample	Crystallite size (nm)	Lattice strain (ε)	XRD intensity ratios		I_{ov}/I_{F2g}	T_{50} (°C)
			[100]/[111]	[110]/[111]		
PDC	8	0.0131	0.321	0.890	0.551	374 ± 0.98
3Ni-PDC	7	0.0150	0.304	0.755	0.612	368 ± 0.45
5Ni-PDC	7	0.0156	0.335	0.717	0.670	366 ± 0.83
7Ni-PDC	6	0.0167	0.304	0.719	0.724	364 ± 0.50
10Ni-PDC	6	0.0165	0.344	0.797	0.847	360 ± 1.20
15Ni-PDC	6	0.0165	0.309	1.118	0.890	361 ± 0.52
20Ni-PDC	6	0.0167	0.285	0.518	0.878	360 ± 1.54

nickel doping and is highest for 10Ni-PDC sample. [110]/[111] facet ratio is found to decrease up to 7 mol% nickel doping in PDC, followed by an increase for 10 and 15 mol% nickel doping. Low facet ratio values observed for 20 mol% nickel doping may be attributed to the formation of the secondary NiO phase. In comparison to (111) plane, (100) and (110) planes have lower oxygen vacancy formation energy and hence are more reactive (Nolan et al. 2005; Aneggi et al. 2014; Andana et al. 2016; Capdevila-Cortada et al. 2016; Patil and Dasari 2019), thus indicating that 10 and 15 mol% Ni-doped PDC samples with highest [100]/[111] and [110]/[111] facet ratios respectively may show better soot oxidation activity.

Figure 2 demonstrates the Raman spectra of *x*Ni-PDC catalysts carried out using a 532 nm laser beam. The Raman band at (450–456) cm^{-1} corresponds to the F_{2g} mode of CeO_2 with O–Ce–O symmetric breathing mode (Keramidas and White 1973; Reddy et al. 2009). The band at (558–573) cm^{-1} corresponds to the oxygen vacancy defects present in *x*Ni-PDC catalysts (McBride et al. 1994; Luo et al. 2006b; Reddy et al. 2009; Martínez-Munuera et al. 2019). For NiO nanopowder, a one phonon band around 570 cm^{-1} corresponding to the presence of defects is the most pronounced, as reported by Mironova-Ulmane et al. (Mironova-Ulmane et al. 2007). Since it overlaps with the oxygen vacancy band of CeO_2, it is difficult to identify bands corresponding to NiO. The intensity ratio of oxygen vacancy peak to the F_{2g} mode peak (I_{ov}/I_{F2g}) tabulated in Table 1 is taken as a parameter to quantify the oxygen vacancies present in all synthesized samples (Luo et al. 2006a; Pu et al. 2007; Reddy et al. 2009). An increase in the relative intensity ratio is noted with the addition of Ni as a dopant. 10, 15, and 20 mol% of Ni doping resulted in almost similar values indicating that the addition of Ni over 10 mol% in the PDC system resulted in the generation of almost constant oxygen vacancies.

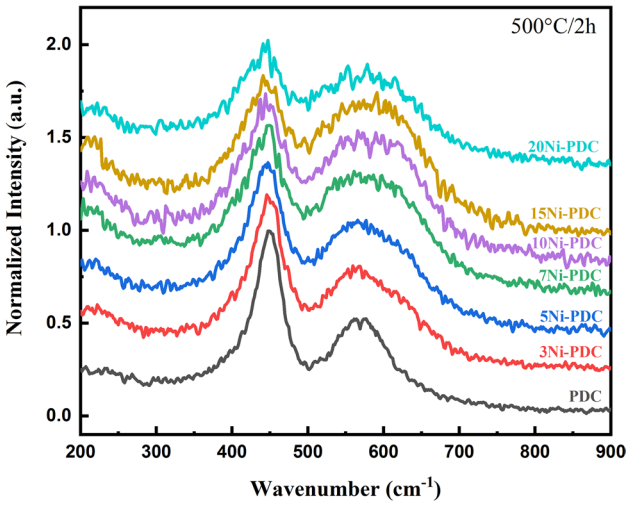

Fig. 2 Raman spectra of all Ni-PDC samples synthesized by SCS calcined at 500 °C/2 h in air

The morphology, particle size, and planes of PDC, 5Ni-PDC, and 10Ni-PDC samples were analyzed by TEM and SAED techniques and are shown in Figs. 3, 4, and 5, respectively. From Figs. 3a, 4a and 5a, agglomerated particles with an irregular elongated shape were observed from PDC, 5Ni-PDC and 10Ni-PDC, respectively. The particle sizes were found to be 6–10 nm for the PDC sample, 4–10 nm for the 5Ni-PDC sample, and 4–7 nm for the 10Ni-PDC sample, which is in the range of the crystallite size calculated from XRD analysis. The lattice spacing calculated from TEM images for PDC (Fig. 3b), 5Ni-PDC (Fig. 4b), and 10Ni-PDC (Fig. 5b) samples correspond to planes of ceria. The SAED patterns for all three samples depict the polycrystalline nature of the samples. (111), (200), (220) and (311) planes from the SAED patterns (Figs. 3c, 4c, and 5c) correspond to the fluorite structure of ceria. No plane corresponding to NiO is observed in both SAED and TEM patterns for

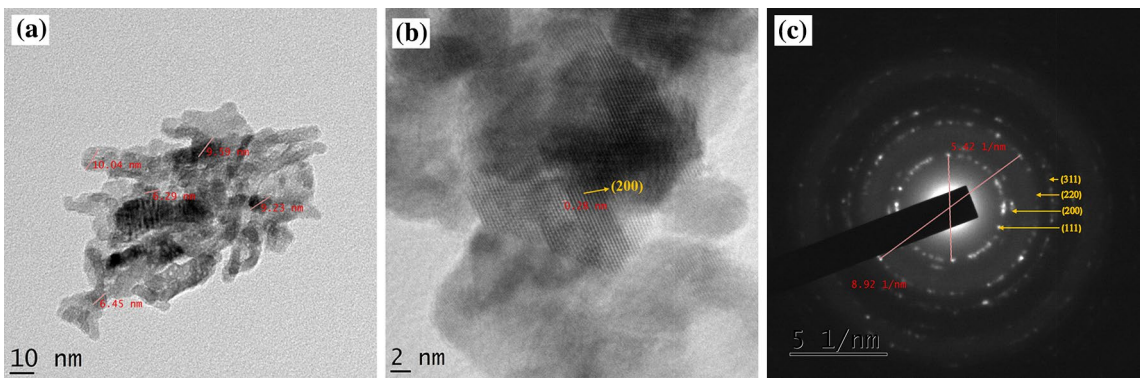

Fig. 3 **a** TEM image, **b** HR-TEM image and **c** SAED pattern of PDC sample synthesized by SCS calcined at 500 °C/2 h in air

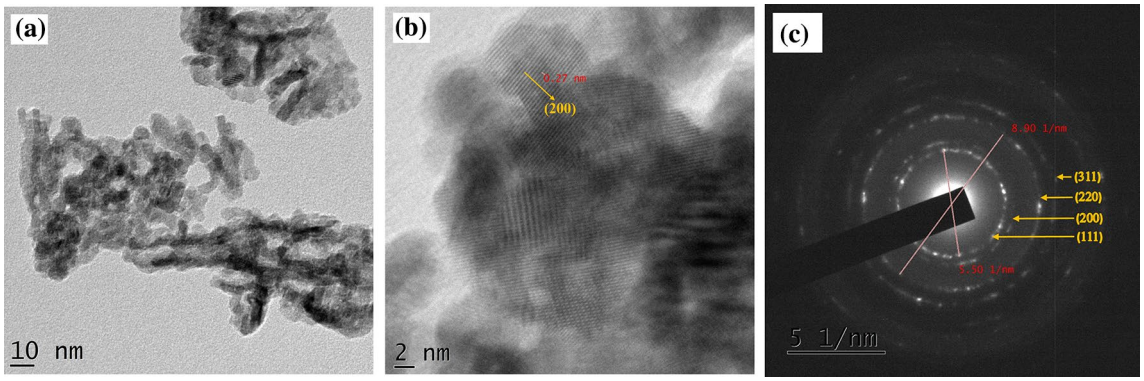

Fig. 4 **a** TEM image, **b** HR-TEM image and **c** SAED pattern of 5Ni-PDC sample synthesized by SCS calcined at 500 °C/2 h in air

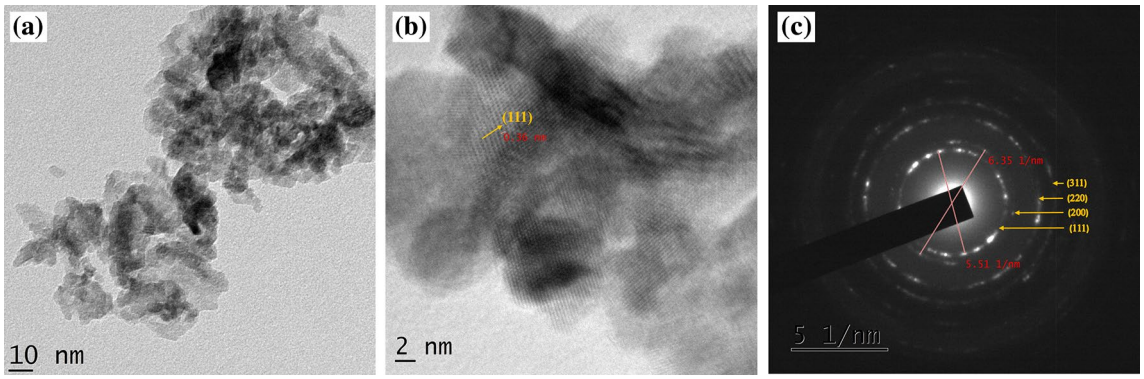

Fig. 5 **a** TEM image, **b** HR-TEM image and **c** SAED pattern of 10Ni-PDC sample synthesized by SCS calcined at 500 °C/2 h in air

PDC, 5Ni-PDC, and 10Ni-PDC samples, as observed in their XRD analysis. From XRD patterns (Fig. 1a), SAED patterns (Figs. 3c, 4c, and 5c) and lattice strain (Table 1), it can be observed that the addition of Ni in PDC catalysts up to 10 mol% resulted in no secondary phase of NiO (from XRD patterns and SAED patterns) and lattice strain increased up to 10Ni-PDC, and further addition has not increased lattice strain. The results confirm that the Ni form a solid-solution with PDC up to the 10Ni-PDC sample.

Figure 6a illustrates the soot oxidation activity of xNi-PDC catalysts, and Table 1 tabulates its corresponding T_{50} temperatures. With the addition of the Ni from 0 to 10 mol% in the PDC system, the T_{50} temperature decreased from 374 to 360 °C, and further addition of Ni (i.e., 15 and 20 mol%) in PDC system haven't decreased the T_{50} temperature further. The soot oxidation activity order is 20Ni-PDC = 15Ni-PDC = 10Ni-PDC > 7Ni-PDC > 5Ni-PDC > 3Ni-PDC > PDC. The T_{50} temperature for catalyzed soot oxidation reactions carried out in the present study is lower than that for uncatalyzed soot oxidation reaction by 200–230 °C.

From the soot oxidation activity results of *x*Ni-PDC catalysts, it can be interpreted that the soot oxidation activity of *x*Ni-PDC catalysts increased with the increase in the Ni mol% from 0 to 10 mol% and a further increase in the Ni mol% have almost no impact on the catalytic activity, thus indicating that the catalytic activity has been saturated and only 10 mol% of Ni is enough to show a better catalytic activity. From XRD analysis and Raman spectroscopy analysis, the lattice strain and relative intensity ratio (I_{ov}/F_{2g}) (Fig. 6b) showed similar trend indicating that the catalytic activity trend followed the lattice strain and oxygen vacancy (relative intensity ratio) and hence the catalytic activity is controlled by the lattice strain and oxygen vacancy xNi-PDC catalysts for soot oxidation.

Table 2 summarizes the information related to the Ni/Ce/Pr catalysts activation energy, T_{50} temperature, and soot

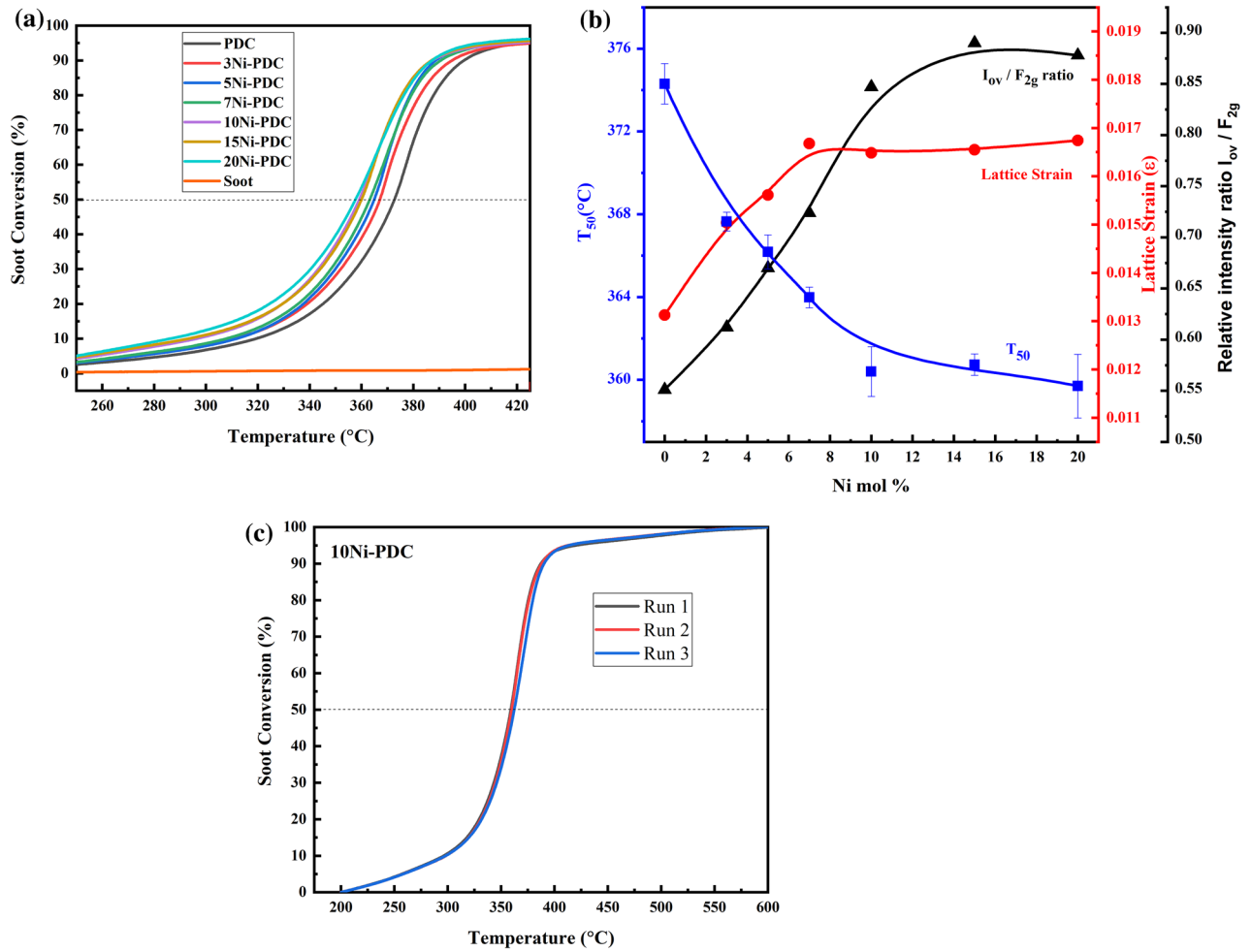

Fig. 6 **a** Soot conversion versus temperature plots for uncatalyzed soot oxidation and catalyzed soot oxidation of *x*Ni-PDC catalysts at 10 °C/min heating rate. **b** Plot of T_{50}, lattice strain and I_{ov}/F_{2g} Raman intensity ratio versus Ni mol%. **c** 10Ni-PDC catalyst reproducibility test for three runs for soot oxidation activity

oxidation experimental conditions obtained from the literature and compared with 10Ni-PDC catalyst performance. Under tight contact mode, 10Ni-PDC catalysts showed better T_{50} temperature than the $Ce_{0.5}Pr_{0.5}O_2$ (nano-fiber) (Jeong et al. 2019), $Ce_{0.9}Pr_{0.1}O_2$ (Jeong et al. 2019), CeO_2 (nanocube) (Jeong et al. 2019), Ce–Pr oxide (Jeong et al. 2019), Ce–Pr oxide (50:50) (nanocube/nanorod) (Andana et al. 2016), CeO_2–Pr_2O_3 (8:2) (Mukherjee et al. 2016), $Ce_{0.8}Pr_{0.2}O_2$ (Thrimurthulu et al. 2012), NiO/CeO_2 (Bendieb Aberkane et al. 2019) and CeO_2 (Palmisano et al. 2006) catalysts. The reason for such kind of better activity can be due to the synthesis method, Ni, and Pr loading in ceria (which controls the physio-chemical properties). *x*Ni-PDC catalysts (360–374 °C) showed much better T_{50} temperature than the perovskite catalysts [BSCF (460 °C), LSCF (500 °C) and LSCM (474 °C)] prepared by reverse co-precipitation method (Shenoy et al. 2019) and Nd and Gd-doped ceria catalysts (427 °C) prepared by glycine-nitrate-process (Anantharaman et al. 2018; Patil et al. 2019). The present study also shows that promotional effect of nickel addition on soot oxidation activity (T_{50} = 360–374 °C) of $Ce_{0.9}Pr_{0.1}O_2$ is better than the promotional effect on soot oxidation activity (T_{50} = 386–410 °C) of cobalt addition to $Ce_{0.5}Zr_{0.5}O_2$ (Zhang et al. 2016).

The activity tests were conducted three times on each catalyst to check the reproducibility of the soot oxidation activity, and T_{50} is almost similar to an error range of less than ± 1.5 °C (see Table 1). Figure 6c shows the soot

Table 2 Comparison of T_{50} temperature, activation energy, and soot oxidation experimental conditions of various Ni/Ce/Pr catalysts

Catalyst	E_a (kJ/mol)	T_{50} (°C)	Soot oxidation experimental conditions	References
$Ce_{0.5}Pr_{0.5}O_2$	–	542	Loose contact, 5% O_2	Guillén-Hurtado et al. (2020)
$Ce_{0.5}Pr_{0.5}O_2$ (nanofiber)	–	388	Tight contact, 100 ml/min air, catalyst/soot = 10:1	Jeong et al. (2019)
Ce–Pr oxide (50:50) (nancube/nanorod)	–	527	Loose contact, 10% O_2	Andana et al. (2018)
$Ce_{0.9}Pr_{0.1}O_2$ oxide	–	398	Tight contact, 50 ml/min 10% O_2, catalyst/soot = 10:1	Zhou et al. (2018)
$Ce_{0.9}Pr_{0.1}O_2$ (nanocube)	–	430	Tight contact, 100 ml/min 10% O_2, catalyst/soot = 9:1	Piumetti et al. (2017)
Ce–Pr oxide	–	413	Tight contact, 50 ml/min 10% O_2, catalyst/soot = 10:1	Fan et al. (2017)
Ce–Pr oxide(50:50) (nancube/nanorod)	–	408	Tight contact, 100 ml/min 50% air + 50% N_2, catalyst/soot = 9:1	Andana et al. (2016)
CeO_2–Pr_2O_3 (8:2)	–	438	Tight contact, 100 ml/min air, catalyst/soot = 4:1	Mukherjee et al. (2016)
$Ce_{0.8}Pr_{0.2}O_{2-\delta}$	–	438	Tight contact, 100 ml/min air, catalyst/soot = 4:1	Thrimurthulu et al. (2012)
NiO/CeO_2	109–133	417	Tight contact, air	Bendieb Aberkane et al. (2019)
Ni/CeO_2 (3DOM)	–	530	Loose contact, 500 ppm NO + 5% O_2	(Sellers-Antón et al. 2020)
Co-Ce oxide (holey nanosheet)	116	311	Tight contact, 5% O_2	Cui et al. (2020)
CeO_2 nanofiber	120	344 (T_{10})	Loose contact, air	Dai et al. (2019)
$Ce_{0.5}Zr_{0.5}O_2$ (3DOM)	51	420	Loose contact, 5% O_2 + 0.2% NO	Xiong et al. (2019)
$20Mn_3O_4/CeO_2$ (microsphere)	130	350	Tight contact, air	Jampaiah et al. (2019)
$Pt@NiO_x/3DOM\text{-}Al_2O_3$ (core–shell nanoparticles)	61	363	Loose contact, 5% O_2, 0.2% NO and 5% H_2O	Wu et al. (2019)
ZnO:CeO_2	54	420	Loose contact, air	Nascimento et al. (2015)
20 wt% Ag/CeO_2	77	266	Tight contact, 20% O_2	Shimizu et al. (2010)
CeO_2	111	405	Tight contact, air	Palmisano et al. (2006)
10Ni-PDC	137	360	Tight contact, air, 100 ml/min, catalyst/soot = 10:1	This study

oxidation activity of 10Ni-PDC catalysts carried out for three runs to check the reproducibility, and each run showed similar activity (change T_{50} is with ± 1.2 °C) and Figure S1 in supplementary information provides the reproducibility of the soot oxidation activity of *x*Ni-PDC catalysts. Since soot oxidation experiments in the present study have been performed inflow of air, the active oxygen mechanism can occur during the soot oxidation process (Guillén-Hurtado et al. 2015).

Soot oxidation activity kinetics is further explored on the PDC, 5Ni-PDC, and 10Ni-PDC catalysts to obtain activation energy, which can further help in analyzing the catalytic activity of synthesized oxides. Figure 7 shows the sigmoidal soot conversion versus temperature curves for all experiments carried out at 5, 10, 15, and 20 °C/min heating rates over PDC (Fig. 7a), 5Ni-PDC (Fig. 7b) and 10Ni-PDC (Fig. 7c) catalysts. The mean activation energy values calculated from linear fits of Ozawa plots shown in Fig. 8 are 133.2 kJ/mol, 133.7 kJ/mol, and 137.3 kJ/mol for PDC (Fig. 8a), 5Ni-PDC (Fig. 8b) and 10Ni-PDC (Fig. 8c) samples. The Ozawa plots have parallel lines for each percentage conversion, indicating a single-step reaction. The activation energy values obtained in the present study are lower than that of non-catalyzed soot oxidation reaction (168 kJ/mol) (Neeft et al. 1997). However, the values of all analyzed catalysts are very close, indicating similar nature and reactivity of active oxygen species facilitated by the synthesized catalysts (Russo et al. 2005; Shimizu et al. 2010). The activation energies of various catalysts for soot oxidation activity is showed in Table 2. The activation energy of 10Ni-PDC (137 kJ/mol) is in a similar range than compared to other catalysts (under tight contact mode) such as Ni/CeO_2 (Bendieb Aberkane et al. 2019), $20Mn_2O_3/CeO_2$ (Jampaiah et al. 2019). The present study shows that the Ni plays a promotional effect in ceria-based catalysts by improving the descriptors such as lattice strain

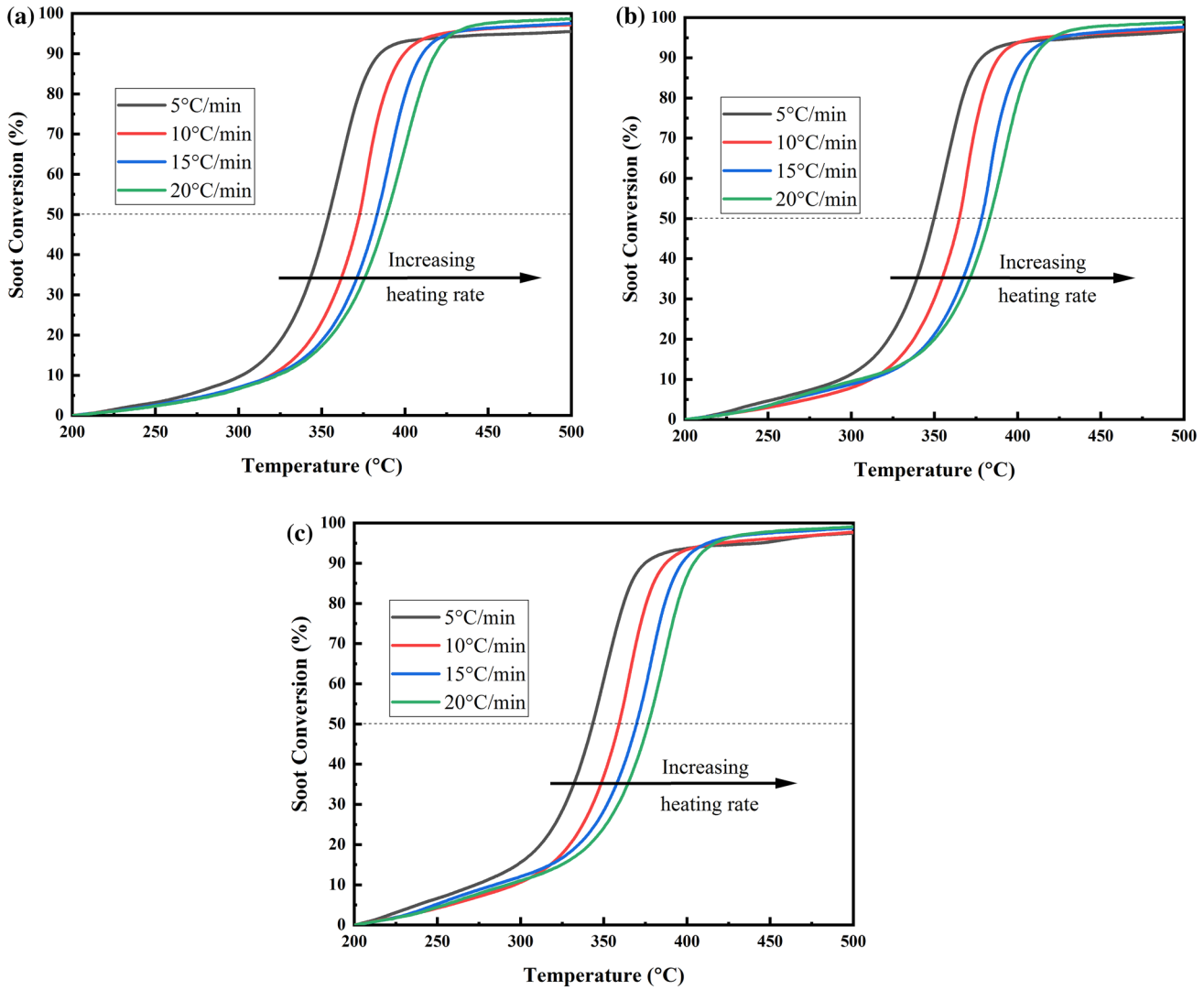

Fig. 7 Soot conversion versus temperature plots at 5, 10, 15, 20 °C/min heating rate for **a** PDC, **b** 5Ni-PDC, **c** 10Ni-PDC catalysts

and oxygen vacancies, which further enhances the soot oxidation activity.

Conclusion

The addition of Ni to $Ce_{0.9}Pr_{0.1}O_2$ oxide catalysts synthesized by solution combustion synthesis method showed a promotional effect on soot oxidation activity. It is shown that nickel doping in PDC positively affects the soot oxidation activity with optimized doping to be 10 mol% of Nickel. 10 mol% nickel doping in PDC catalyst reduced the T_{50} temperature from 374 °C for PDC to 360 °C for 10Ni-PDC, which has been attributed to increased lattice strain and oxygen vacancies. From XRD and SAED patterns, it is confirmed that up to 10 mol% Ni addition in PDC catalysts resulted in the formation of solid-solution and thus increased the oxygen vacancies, which is observed from Raman spectroscopy. For the 10Ni-PDC catalyst, from soot oxidation kinetic studies, the activation energy obtained from Ozawa plots is 137 kJ/mol.

Acknowledgements A part of the research work is funded by the SERB-IMPRINT-II (IMP/2018/001318) project titled "Development and demonstration of solid oxide electrolysis cell technology for co-electrolysis of CO_2 and H_2O for the production of syngas". We acknowledge SAIF STIC, Cochin, as well as MRC, MNIT Jaipur, for providing TEM analysis data and Raman spectroscopy data, respectively.

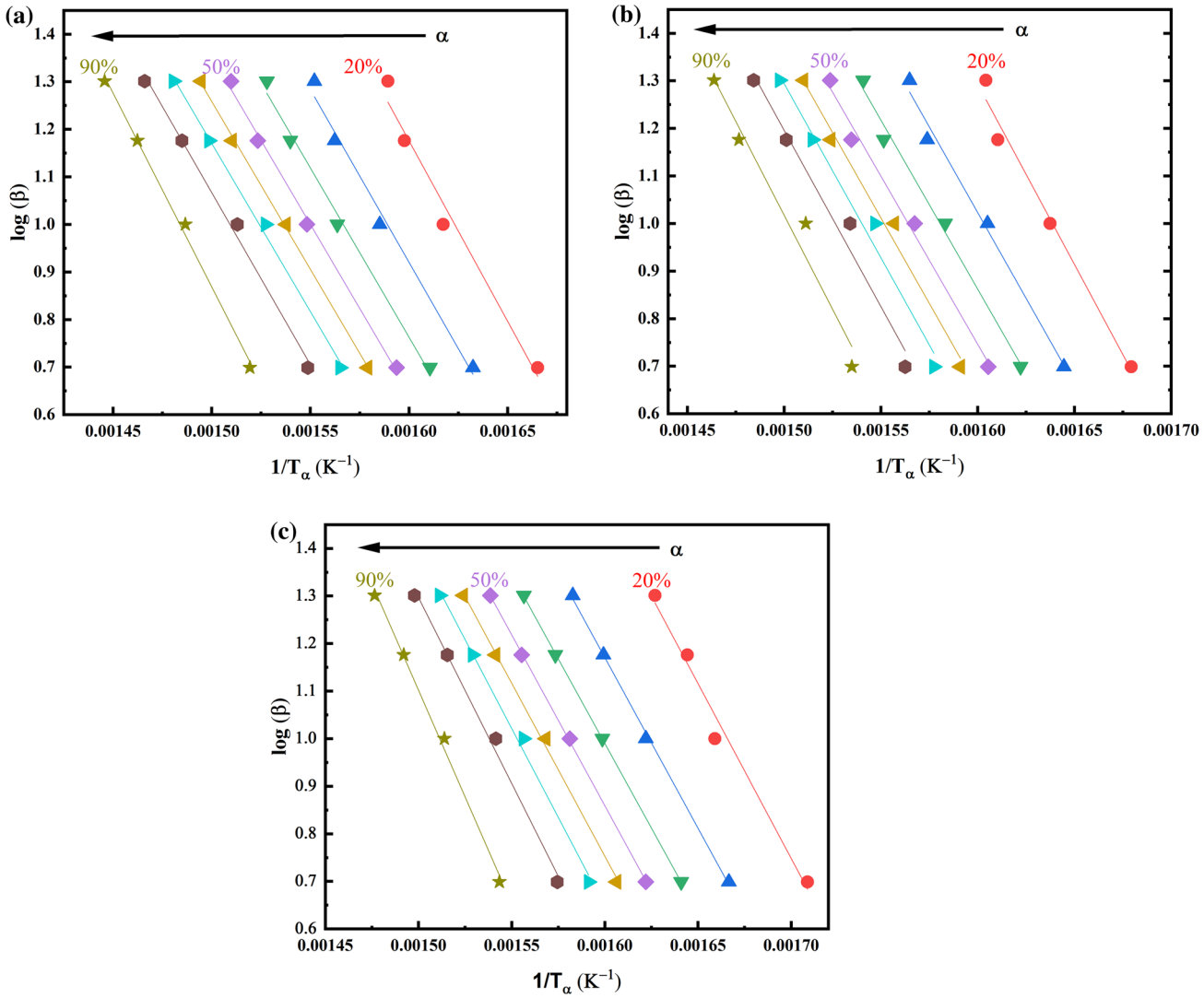

Fig. 8 Ozawa plots for **a** PDC, **b** 5Ni-PDC, **c** 10Ni-PDC catalysts

References

Abu-Zied BM, Mohamed YA, Asiri AM (2013) Fabrication, characterization, and electrical conductivity properties of Pr_6O_{11} nanoparticles. J Rare Earths 31:701–708. https://doi.org/10.1016/S1002-0721(12)60345-7

Adler J (2005) Ceramic diesel particulate filters. Int J Appl Ceram Technol 2:429–439. https://doi.org/10.1111/j.1744-7402.2005.02044.x

Álvarez-Docio CM, Portela R, Reinosa JJ et al (2020) Performance and stability of wet-milled $CoAl_2O_4$, Ni/$CoAl_2O_4$, and Pt, Ni/$CoAl_2O_4$ for soot combustion. Catalysts 10:406. https://doi.org/10.3390/catal10040406

Alvarez-Galvan C, Melian M, Ruiz-Matas L et al (2019) Partial oxidation of methane to syngas over nickel-based catalysts: influence of support type, addition of rhodium, and preparation method. Front Chem 7:104. https://doi.org/10.3389/fchem.2019.00104

Anantharaman AP, Gadiyar HJ, Surendran M et al (2018) Effect of synthesis method on structural properties and soot oxidation activity of gadolinium-doped ceria. Chem Pap 72:3179–3188. https://doi.org/10.1007/s11696-018-0532-5

Andana T, Piumetti M, Bensaid S et al (2016) Nanostructured ceria-praseodymia catalysts for diesel soot combustion. Appl Catal B Environ 197:125–137. https://doi.org/10.1016/j.apcatb.2015.12.030

Andana T, Piumetti M, Bensaid S et al (2018) Nanostructured equimolar ceria-praseodymia for NO_x-assisted soot oxidation: insight into Pr dominance over Pt nanoparticles and metal–support interaction. Appl Catal B Environ 226:147–161. https://doi.org/10.1016/j.apcatb.2017.12.048

Aneggi E, Llorca J, de Leitenburg C et al (2009) Soot combustion over silver-supported catalysts. Appl Catal B Environ 91:489–498. https://doi.org/10.1016/j.apcatb.2009.06.019

Aneggi E, Wiater D, De Leitenburg C et al (2014) Shape-dependent activity of ceria in soot combustion. ACS Catal 4:172–181. https://doi.org/10.1021/cs400850r

Atribak I, Bueno-López A, García-García A (2008) Thermally stable ceria-zirconia catalysts for soot oxidation by O2. Catal Commun 9:250–255. https://doi.org/10.1016/j.catcom.2007.05.047

Bendieb Aberkane A, Yeste MP, Fayçal D et al (2019) Catalytic soot oxidation activity of NiO–CeO_2 catalysts prepared by a coprecipitation method: influence of the preparation ph on the catalytic performance. Materials (Basel) 12:3436. https://doi.org/10.3390/ma12203436

Bindu P, Thomas S (2014) Estimation of lattice strain in ZnO nanoparticles: X-ray peak profile analysis. J Theor Appl Phys 8:123–134. https://doi.org/10.1007/s40094-014-0141-9

Bueno-López A (2014) Diesel soot combustion ceria catalysts. Appl Catal B Environ 146:1–11. https://doi.org/10.1016/j.apcatb.2013.02.033

Bueno-López A, Krishna K, Makkee M, Moulijn JA (2005) Active oxygen from CeO_2 and its role in catalysed soot oxidation. Catal Lett 99:203–205. https://doi.org/10.1007/s10562-005-2120-x

Capdevila-Cortada M, Vilé G, Teschner D et al (2016) Reactivity descriptors for ceria in catalysis. Appl Catal B Environ 197:299–312. https://doi.org/10.1016/j.apcatb.2016.02.035

Chen HI, Chang HY (2005) Synthesis and characterization of nanocrystalline cerium oxide powders by two-stage non-isothermal precipitation. Solid State Commun 133:593–598. https://doi.org/10.1016/j.ssc.2004.12.020

Cui B, Zhou L, Li K et al (2020) Holey Co–Ce oxide nanosheets as a highly efficient catalyst for diesel soot combustion. Appl Catal B Environ 267:118670. https://doi.org/10.1016/j.apcatb.2020.118670

Dai Y, Tian J, Fu W (2019) Shape manipulation of porous CeO2 nanofibers: facile fabrication, growth mechanism and catalytic elimination of soot particulates. J Mater Sci 54:10141–10152. https://doi.org/10.1007/s10853-019-03648-9

Ding M, Yang H, Yan T et al (2018) Fabrication of hierarchical ZnO@NiO core-shell heterostructures for improved photocatalytic performance. Nanoscale Res Lett 13:260. https://doi.org/10.1186/s11671-018-2676-1

Fan L, Xi K, Zhou Y, et al (2017) Design structure for CePr mixed oxide catalysts in soot combustion †. https://doi.org/10.1039/c6ra28722k

Giménez-Mañogil J, Bueno-López A, García-García A (2014) Preparation, characterisation and testing of $CuO/Ce_{0.8}Zr_{0.2}O_2$ catalysts for NO oxidation to NO_2 and mild temperature diesel soot combustion. Appl Catal B Environ 152–153:99–107. https://doi.org/10.1016/j.apcatb.2014.01.018

Govindhan M, Sidhureddy B, Chen A (2018) High-temperature hydrogen gas sensor based on three-dimensional hierarchical-nanostructured nickel-cobalt oxide. ACS Appl Nano Mater 1:6005–6014. https://doi.org/10.1021/acsanm.8b00835

Grabchenko MV, Mamontov GV, Zaikovskii VI et al (2020) The role of metal–support interaction in Ag/CeO_2 catalysts for CO and soot oxidation. Appl Catal B Environ 260:118148. https://doi.org/10.1016/j.apcatb.2019.118148

Guillén-Hurtado N, García-García A, Bueno-López A (2015) Active oxygen by Ce–Pr mixed oxide nanoparticles outperform diesel soot combustion Pt catalysts. Appl Catal B Environ 174–175:60–66. https://doi.org/10.1016/j.apcatb.2015.02.036

Guillén-Hurtado N, Giménez-Mañogil J, Martínez-Munuera JC et al (2020) Study of Ce/Pr ratio in ceria-praseodymia catalysts for soot combustion under different atmospheres. Appl Catal A Gen. https://doi.org/10.1016/j.apcata.2019.117339

Hauch A, Brodersen K, Chen M, Mogensen MB (2016) Ni/YSZ electrodes structures optimized for increased electrolysis performance and durability. Solid State Ion 293:27–36. https://doi.org/10.1016/j.ssi.2016.06.003

Jampaiah D, Velisoju VK, Devaiah D et al (2019) Flower-like Mn_3O_4/CeO_2 microspheres as an efficient catalyst for diesel soot and CO oxidation: synergistic effects for enhanced catalytic performance. Appl Surf Sci 473:209–221. https://doi.org/10.1016/j.apsusc.2018.12.048

Jeong EJ, Lee JH, Lee SH et al (2019) Ce–Pr mixed oxide catalysts with a fibrous morphology for low-temperature PM oxidation. ChemCatChem 11:2131–2141. https://doi.org/10.1002/cctc.201802011

Kayama T, Yamazaki K, Shinjoh H (2010) Nanostructured ceria-silver synthesized in a one-pot redox reaction catalyzes carbon oxidation. J Am Chem Soc 132:13154–13155. https://doi.org/10.1021/ja105403x

Kehoe AB, Scanlon DO, Watson GW (2011) Role of lattice distortions in the oxygen storage capacity of divalently doped ceo_2. Chem Mater 23:4464–4468. https://doi.org/10.1021/cm201617d

Keramidas VG, White WB (1973) Raman spectra of oxides with the fluorite structure. J Chem Phys 59:1561–1562

Lim CB, Kusaba H, Einaga H, Teraoka Y (2011) Catalytic performance of supported precious metal catalysts for the combustion of diesel particulate matter. In: Catalysis today. Elsevier B.V., pp 106–111

Liu S, Wu X, Weng D, Ran R (2015) Ceria-based catalysts for soot oxidation: a review. J Rare Earths 33:567–590

Liu F, Sang Y, Ma H et al (2017) Nickel oxide as an effective catalyst for catalytic combustion of methane. J Nat Gas Sci Eng 41:1–6. https://doi.org/10.1016/j.jngse.2017.02.025

Lo Nigro R, Toro RG, Malandrino G et al (2003) A simple route to the synthesis of Pr_2O_3 high-k thin films. Adv Mater 15:1071–1075

Luo M-F, Yan Z-L, Jin L-Y, He M (2006a) Raman spectroscopic study on the structure in the surface and the bulk shell of Ce x Pr $1-x$ O_2 - δ Mixed Oxides. J Phys Chem B 110:13068–13071. https://doi.org/10.1021/jp057274z

Luo MF, Yan ZL, Jin LY (2006b) Structure and redox properties of $Ce_xPr_{1-x}O_{2-\delta}$ mixed oxides and their catalytic activities for CO, CH_3OH and CH_4 combustion. J Mol Catal A Chem 260:157–162. https://doi.org/10.1016/j.molcata.2006.07.012

Machida M, Murata Y, Kishikawa K et al (2008) On the reasons for high activity of CeO_2 catalyst for soot oxidation. Chem Mater 20:4489–4494. https://doi.org/10.1021/cm800832w

Martínez-Munuera JC, Zoccoli M, Giménez-Mañogil J, García-García A (2019) Lattice oxygen activity in ceria-praseodymia mixed oxides for soot oxidation in catalysed Gasoline Particle Filters. Appl Catal B Environ 245:706–720. https://doi.org/10.1016/j.apcatb.2018.12.076

Matović B, Pantić J, Prekajski M et al (2013) Synthesis and characterization of Pr_6O_{11} nanopowders. Ceram Int 39:3151–3155. https://doi.org/10.1016/j.ceramint.2012.09.098

McBride JR, Hass KC, Poindexter BD, Weber WH (1994) Raman and X-ray studies of $Ce_{1-x}RE_xO_{2-y}$, where RE = La, Pr, Nd, Eu, Gd, and Tb. J Appl Phys 76:2435–2441. https://doi.org/10.1063/1.357593

Miniach E, Śliwak A, Moyseowicz A, Gryglewicz G (2016) Growth of carbon nanofibers from methane on a hydroxyapatite-supported nickel catalyst. J Mater Sci 51:5367–5376. https://doi.org/10.1007/s10853-016-9839-1

Mironova-Ulmane N, Kuzmin A, Steins I et al (2007) Raman scattering in nanosized nickel oxide NiO. J Phys Conf Ser. https://doi.org/10.1088/1742-6596/93/1/012039

Mukherjee D, Reddy BM (2018) Noble metal-free CeO_2-based mixed oxides for CO and soot oxidation. Catal Today 309:227–235. https://doi.org/10.1016/j.cattod.2017.06.017

Mukherjee D, Rao BG, Reddy BM (2016) CO and soot oxidation activity of doped ceria: influence of dopants. Appl Catal B Environ 197:105–115. https://doi.org/10.1016/j.apcatb.2016.03.042

Nascimento LF, Martins RF, Serra OA (2014) Catalytic combustion of soot over Ru-doped mixed oxides catalysts. J Rare Earths 32:610–620. https://doi.org/10.1016/S1002-0721(14)60116-2

Nascimento LF, De Sousa Filho PC, Lima JF, Serra OA (2015) Kinetic parameters of soot oxidation catalyzed by nanosized ZnO–CeO_2 solids. J Braz Chem Soc 26:1315–1320. https://doi.org/10.5935/0103-5053.20150098

Neeft JPA, Nijhuis TX, Smakman E et al (1997) Kinetics of the oxidation of diesel soot. Fuel 76:1129–1136. https://doi.org/10.1016/S0016-2361(97)00119-1

Neelapala SD, Patnaik H, Dasari H (2018) Enhancement of soot oxidation activity of manganese oxide (Mn_2O_3) through doping by the formation of $Mn_{1.9}M_{0.1}O_{3-\delta}$ (M = Co, Cu, and Ni). Asia Pac J Chem Eng 13:e2234. https://doi.org/10.1002/apj.2234

Nolan M, Parker SC, Watson GW (2005) The electronic structure of oxygen vacancy defects at the low index surfaces of ceria. Surf Sci 595:223–232. https://doi.org/10.1016/j.susc.2005.08.015

Palmisano P, Russo N, Fino D, Badini C (2006) Solution combustion synthesis boosts ceria activity towards diesel soot combustion. In: AIChE annual meeting, conference proceedings

Patil S, Dasari HP (2019) Effect of fuel and solvent on soot oxidation activity of ceria nanoparticles synthesized by solution combustion method. Mater Sci Energy Technol 2:485–489. https://doi.org/10.1016/j.mset.2019.05.005

Patil SS, Dasari HP, Dasari H (2019) Effect of Nd-doping on soot oxidation activity of ceria-based nanoparticles synthesized by glycine nitrate process. Nano-Struct Nano-Obj 20:100388. https://doi.org/10.1016/j.nanoso.2019.100388

Pischinger F, Lepperhoff G, Houben M (1994) Soot formation and oxidation in diesel engines. Springer, Berlin

Piumetti M, Andana T, Bensaid S et al (2017) Ceria-based nanomaterials as catalysts for CO oxidation and soot combustion: effect of Zr–Pr doping and structural properties on the catalytic activity. AIChE J 63:216–225. https://doi.org/10.1002/aic.15548

Pu Z-Y, Lu J-Q, Luo M-F, Xie Y-L (2007) Study of oxygen vacancies in $Ce_{0.9}$ $Pr_{0.1}$ $O_{2-\delta}$ solid solution by in situ X-ray diffraction and in situ Raman spectroscopy. J Phys Chem C 111:18695–18702. https://doi.org/10.1021/jp0759776

Putla S, Amin MH, Reddy BM et al (2015) MnO_x nanoparticle-dispersed CeO_2 nanocubes: a remarkable heteronanostructured system with unusual structural characteristics and superior catalytic performance. ACS Appl Mater Interfaces 7:16525–16535. https://doi.org/10.1021/acsami.5b03988

Ramanathan V, Carmichael G (2008) Global and regional climate changes due to black carbon. Nat Geosci 1:221–227

Rao KN, Venkataswamy P, Reddy BM (2011) Structural characterization and catalytic evaluation of supported copper-ceria catalysts for soot oxidation. Ind Eng Chem Res 50:11960–11969. https://doi.org/10.1021/ie201474p

Reddy BM, Thrimurthulu G, Katta L et al (2009) Structural characteristics and catalytic activity of nanocrystalline ceria–praseodymia solid solutions. J Phys Chem C 113:15882–15890. https://doi.org/10.1021/jp903644y

Rico-Pérez V, Aneggi E, Bueno-López A, Trovarelli A (2016) Synergic effect of Cu/$Ce_{0.5}Pr_{0.5}O_{2-\delta}$ and $Ce_{0.5}Pr_{0.5}O_{2-\delta}$ in soot combustion. Appl Catal B Environ 197:95–104. https://doi.org/10.1016/j.apcatb.2016.02.051

Ristovski ZD, Miljevic B, Surawski NC et al (2012) Respiratory health effects of diesel particulate matter. Respirology 17:201–212. https://doi.org/10.1111/j.1440-1843.2011.02109.x

Rushton MJD, Chroneos A (2014) Impact of uniaxial strain and doping on oxygen diffusion in CeO_2. Sci Rep. https://doi.org/10.1038/srep06068

Russo N, Fino D, Saracco G, Specchia V (2005) Studies on the redox properties of chromite perovskite catalysts for soot combustion. J Catal 229:459–469. https://doi.org/10.1016/j.jcat.2004.11.025

Sellers-Antón B, Bailón-García E, Cardenas-Arenas A et al (2020) Enhancement of the generation and transfer of active oxygen in Ni/CeO_2 catalysts for soot combustion by controlling the Ni–ceria contact and the three-dimensional structure. Environ Sci Technol 54:2439–2447. https://doi.org/10.1021/acs.est.9b07682

Setiabudi A, Chen J, Mul G et al (2004) CeO_2 catalysed soot oxidation: the role of active oxygen to accelerate the oxidation conversion. Appl Catal B Environ 51:9–19. https://doi.org/10.1016/j.apcatb.2004.01.005

Shen Q, Lu G, Du C et al (2013) Role and reduction of NO_x in the catalytic combustion of soot over iron-ceria mixed oxide catalyst. Chem Eng J 218:164–172. https://doi.org/10.1016/j.cej.2012.12.010

Shenoy CS, Patil SS, Govardhan P et al (2019) Studies on the solid oxide cell perovskite electrode materials for soot oxidation activity. Emiss Control Sci Technol 5:342–352. https://doi.org/10.1007/s40825-019-00144-z

Shimizu K, Kawachi H, Satsuma A (2010) Study of active sites and mechanism for soot oxidation by silver-loaded ceria catalyst. Appl Catal B Environ 96:169–175. https://doi.org/10.1016/j.apcatb.2010.02.016

Singh A, Chang SLY, Hocking RK et al (2013) Highly active nickel oxide water oxidation catalysts deposited from molecular complexes. Energy Environ Sci 6:579–586. https://doi.org/10.1039/c2ee23862d

Singhania A, Gupta SM (2017) Nickel nanocatalyst ex-solution from ceria-nickel oxide solid solution for low temperature CO oxidation. J Nanosci Nanotechnol 18:4614–4620. https://doi.org/10.1166/jnn.2018.15342

Sudarsanam P, Hillary B, Deepa DK et al (2015) Highly efficient cerium dioxide nanocube-based catalysts for low temperature diesel soot oxidation: the cooperative effect of cerium- and cobalt-oxides. Catal Sci Technol 5:3496–3500. https://doi.org/10.1039/c5cy00525f

Sydbom A, Blomberg A, Parnia S et al (2001) Health effects of diesel exhaust emissions. Eur Respir J 17:733–746. https://doi.org/10.1183/09031936.01.17407330

Thrimurthulu G, Rao KN, Devaiah D, Reddy BM (2012) Nanocrystalline ceria-praseodymia and ceria-zirconia solid solutions for soot oxidation. Res Chem Intermed 38:1847–1855. https://doi.org/10.1007/s11164-012-0508-y

Tok AIY, Du SW, Boey FYC, Chong WK (2007) Hydrothermal synthesis and characterization of rare earth doped ceria nanoparticles. Mater Sci Eng A 466:223–229. https://doi.org/10.1016/j.msea.2007.02.083

Uppara HP, Feroz A, John NS, et al (2019) Soot oxidation studies on $SrMn_{0.98}B_{0.02}O_3$ (B - Fe, Ni) perovskites. In: IOP conference series: materials science and engineering

Venkataswamy P, Jampaiah D, Rao KN, Reddy BM (2014) Nanostructured $Ce_{0.7}Mn_{0.3}O_{2-\delta}$ and $Ce_{0.7}Fe_{0.3}O_{2-\delta}$ solid solutions for diesel soot oxidation. Appl Catal A Gen 488:1–10. https://doi.org/10.1016/j.apcata.2014.09.014

Venugopal A, Naveen Kumar S, Ashok J et al (2007) Hydrogen production by catalytic decomposition of methane over Ni/SiO_2. Int J Hydrogen Energy 32:1782–1788. https://doi.org/10.1016/j.ijhydene.2007.01.007

Wu Q, Jing M, Wei Y et al (2019) High-efficient catalysts of core-shell structured Pt@transition metal oxides (TMOs) supported on 3DOM-Al_2O_3 for soot oxidation: the effect of strong Pt-TMO interaction. Appl Catal B Environ 244:628–640. https://doi.org/10.1016/j.apcatb.2018.11.094

Xin Q (2013) The analytical design process and diesel engine system design. Diesel engine system design. Elsevier, Oxford, pp 3–112

Xiong J, Wei Y, Zhang Y et al (2019) Facile synthesis of 3D ordered macro-mesoporous $Ce_{1-x}Zr_xO_2$ catalysts with enhanced catalytic activity for soot oxidation. Catal Today. https://doi.org/10.1016/j.cattod.2019.05.061

Xu J, Lu G, Guo Y et al (2017) A highly effective catalyst of Co-CeO_2 for the oxidation of diesel soot: the excellent NO oxidation activity and NO*x* storage capacity. Appl Catal A Gen 535:1–8. https://doi.org/10.1016/j.apcata.2017.02.005

Yadav BC, Singh M, Dwivedi CD (2011) Optical characterization and humidity sensing properties of praseodymium oxide. Sens Transducers 125:68–75

Zeng L, Cui L, Wang C et al (2020) In-situ modified the surface of Pt-doped perovskite catalyst for soot oxidation. J Hazard Mater 383:121210. https://doi.org/10.1016/j.jhazmat.2019.121210

Zhang YH, Zhang HL, Cao Y et al (2016) Promotional effect of cobalt addition on catalytic performance of $Ce_{0.5}Zr_{0.5}O_2$ mixed oxide for diesel soot combustion. Chem Pap 70:1370–1379. https://doi.org/10.1515/chempap-2016-0070

Zhao M, Deng J, Liu J et al (2019) Roles of surface-active oxygen species on 3DOM cobalt-based spinel catalysts $M_xCo_{3-x}O_4$ (M = Zn and Ni) for NO_x-assisted soot oxidation. ACS Catal 9:7548–7567. https://doi.org/10.1021/acscatal.9b01995

Zhou L, Li X, Yao Z et al (2016) Transition-Metal Doped Ceria Microspheres With Nanoporous Structures for CO oxidation. Sci Rep. https://doi.org/10.1038/srep23900

Zhou B, Xi K, Fan LJ et al (2018) A comparative study on Ce–Pr and Ce–Mn mixed oxide catalysts toward soot catalytic combustion. Appl Catal A Gen 562:1–10. https://doi.org/10.1016/j.apcata.2018.05.034